

3D Shape Reconstruction of Small Bodies From Sparse Features

Benjamin Jarvis , Gary P. T. Choi , Benjamin Hockman, Benjamin Morrell , Saptarshi Bandopadhyay , Daniel Lubey, Jacopo Villa, Shyam Bhaskaran, David Bayard, and Issa A. Nesnas

Abstract—The autonomous approach of spacecraft to a small body (comet or asteroid) relies on using all available information at each phase of the approach. This letter presents new algorithms for global shape reconstructions from sparse tracked surface points. These methods leverage estimates from earlier phases, such as rotation pole, as well as *a priori* knowledge, such as a genus-0 body (i.e. without boundaries or topological holes). A mapping algorithm is proposed, which performs faithful reconstructions while enforcing genus-0 output through spherical parameterization. To estimate the shape of permanently shadowed regions of the body, a symmetry reconstruction method is added to the reconstruction algorithms. This method is shown to substantially increase the reconstruction accuracy but is subject to the symmetry of the body perpendicular to the rotation pole. The proposed mapping algorithm is compared to state-of-the-practice surface reconstruction algorithms, assessing their accuracy and ability to correctly generate genus-0 shape models for 2400 datasets and three small bodies. The proposed spherical parameterization algorithm performed consistently with the state-of-the-practice while being the only algorithm to always produce genus-0 shape models.

Index Terms—Mapping, computational geometry, computer vision for automation.

I. INTRODUCTION

THE exploration of small celestial Near-Earth bodies (asteroids and comets) benefits scientific exploration and enables the development of technologies for future applications such as *in-situ* resource utilization and planetary defence. The interest in small-body exploration is evident from recent missions, such as NASA’s OSIRIS-REX, ESA’s Rosetta, and JAXA’s Hayabusa missions. Operating these missions require extensive planning

Manuscript received February 24, 2021; accepted June 25, 2021. Date of publication July 14, 2021; date of current version July 28, 2021. This work was supported in part by the Jet Propulsion Laboratory, California Institute of Technology, under a contract with National Aeronautics and Space Administration under Grant 80NM0018D0004 and in part by the National Science Foundation under Grant DMS-2002103 (to G. P. T. Choi). (Corresponding author: Benjamin Jarvis.)

Benjamin Jarvis is with the School of Aerospace, Mechanical, and Mechatronic Engineering, The University of Sydney, Camperdown, NSW 2006, Australia (e-mail: ben_jarvis@outlook.com).

Gary P. T. Choi is with the Department of Mathematics, Massachusetts Institute of Technology, Cambridge, MA 02139 USA (e-mail: ptchoi@mit.edu).

Benjamin Hockman, Benjamin Morrell, Saptarshi Bandopadhyay, Daniel Lubey, Jacopo Villa, Shyam Bhaskaran, David Bayard, and Issa A. Nesnas are with the Jet Propulsion Laboratory, California Institute of Technology, Pasadena, CA 91109 USA (e-mail: benhockman63@gmail.com; benjamin.morrell@jpl.nasa.gov; bandyop2@illinois.edu; daniel.p.lubey@jpl.nasa.gov; jacobov@kth.se; shyamkumar.bhaskaran@jpl.nasa.gov; david.s.bayard@jpl.nasa.gov; nesnas@jpl.nasa.gov).

Digital Object Identifier 10.1109/LRA.2021.3097273

and countless person-hours to accomplish. Due to this, there is growing motivation to leverage spacecraft autonomy to enable further and more frequent exploration of small bodies, at a lower cost. An essential part of enabling this is accurate and robust shape reconstruction of the target body during approach.

An autonomous approach pipeline consists of a number of different phases; at each step there is an effort to leverage all available information to further inform the approach [1]. We focus here on the phase of the approach when visual features are first able to be reliably tracked, generating a coarse set of corresponding 100–1000 3D landmarks that form a sparse point cloud representing the small body [2]. We aim to generate a global 3D map of the small body, leveraging all available prior information, primarily, the 3D landmarks and pole of rotation (determined through pole-from-silhouette algorithms [3]). The goal for the resulting global shape model is to enable initial gravity estimates and to inform a future dense-mapping phase. A particular requirement for gravity estimation is to have a *watertight*, genus-0 surface (i.e., a spherical topology).

Throughout the approach, there is a desire to track fewer but more accurate features for longer durations in order to reduce uncertainties in the orbit determination. Therefore, coarse shape reconstruction is performed with fewer features, especially in the earlier phases of the approach. Shape reconstruction using sparse data can produce inconsistent results using existing mapping approaches. One notable inconsistency is the generation of shapes with non-spherical topologies, a situation where the reconstructed shape of the body has holes or results in multiple incorrect separate bodies (non-genus-0). To address these challenges, we propose a mapping algorithm that is robust to sparse data and guarantees a genus-0 reconstruction. We present an analysis of this algorithm along with the existing state-of-the-practice methods for coarse watertight reconstruction.

Another challenge that is specific to mapping small celestial bodies is the presence of large permanently shadowed regions, which are never visible. To address the lack of information in these shadowed regions, we propose a technique for “filling in” these regions with artificial points that are inferred from an assumption of symmetry and our knowledge of the rotation pole.

II. RELATED WORK

The mapping of small bodies is an extensively studied problem with various techniques for producing accurate Digital Terrain Maps (DTMs) [4]. Stereo Photoclinometry (SPC) is

the most widely used method due to its ability to model the topography and light source to produce accurate DTMs while simultaneously refining the pose estimate [5], [6]. However, this is a human-intensive process that relies on extensive ground analysis and communication with the spacecraft, limiting its use in autonomous operations [1]. The use of Simultaneous Localization and Mapping (SLAM) techniques for small-body mapping has been explored in recent years, however, these have primarily relied on range sensors [7] or have suggested incorporating ground-based measurements [8], which constrains operations. While additional data from earlier phases could be incorporated, such as visual-hull shapes reconstructed from observing the body's silhouettes [3], this paper focuses on the feasibility of solely using landmarks from feature tracking. Promising results have been found with landmark only methods [9], however, this analysis did not construct a mesh and used randomly sampled landmarks that did not account for any permanently shadowed regions.

Over the past several decades, there has been a large body of work on surface reconstruction and mapping of point clouds [10]–[12]. The “Cocone” algorithm [13] constructs the 3D Voronoi diagram for the point cloud and filters out points using conical constraints defined by each point's surface normal, followed by a Delaunay triangulation to connect neighbouring points. “Tight Cocone” [14] is a variant for reconstructing watertight surfaces which performs imperfect hole closing by peeling the convex hull. The “Powercrust” method [15] grows spheres from the vertices of the Voronoi diagram that are interior to the body until they intersect the point cloud. The process is repeated for the exterior vertices and the points formed from the intersection of these interior and exterior spheres forms a watertight estimate of the surface. These intersection points are then triangulated using the Delaunay method. “Poisson surface reconstruction” [16] requires the estimated surface normal of landmarks to form a continuous vector field to generate an isosurface. The vector field is an approximation of the gradient of the indicator function, a binary function that identifies points inside the body, which is derived by solving a Laplace equation. While these methods have proven to be highly effective for many science and engineering applications, they either change the position of input points, produce a mesh with topological holes, or both.

To take the topology of the input point clouds into consideration in the mapping and meshing process, one common approach is to make use of point cloud parameterization [17], [18]. In particular, Choi *et al.* [19] proposed a method for meshing point clouds with spherical topology via spherical conformal parameterization. The method generates a faithful triangular mesh based on the input points without introducing new points or changing the position of the input points. The resulting mesh is guaranteed to be genus-0. However, the method primarily focuses on dense point clouds and does not produce accurate reconstructions for coarse point clouds, this will be shown in Section VI-B.

Applying symmetry assumptions for shape reconstruction from partial visibility is an extensive area of research applied to a range of applications. It has been proposed for non-invasive

model generation in biomedicine [20], and widely investigated for scene reconstruction to aid in 3D mapping [21], and grasping [22]. Much of this research focuses on the detection of symmetry, whether that relies on user input and prior knowledge [23], or is computed with no prior [24], [25]. To determine the symmetry planes, these methods all rely on having high accuracy and dense partial reconstructions of the shape, which enables precise detection of any symmetry and accurate reconstruction of the occluded regions. An equatorial symmetry assumption was applied to improve the initial volume estimate of Comet 67P, to construct unobserved regions in the southern hemisphere [26].

III. SPHERICAL PARAMETERIZATION

In this section, we develop a novel spherical parameterization method for coarse point clouds and use it for surface reconstruction (see Fig. 1). Our proposed method primarily follows the prior approach [19], with modifications in several key steps for improving the performance. Note that directly mapping the point clouds onto a sphere is difficult because of their shape variation. Therefore, we achieve a spherical parameterization by first mapping a point cloud onto the 2D plane, and then map the plane onto the unit sphere.

The first step of the proposed algorithm is to approximate the Laplacian on the input point cloud (denoted as $\mathcal{P} = \{v_i\}_{i=1}^n$, where n is the total number of points). Note that in the prior method [19], the Laplacian is approximated using the moving least squares (MLS) method, which involves the approximation of higher order derivatives and hence does not work well for coarse point clouds and may significantly affect the subsequent computation (see Section VI for experimental results). Therefore, here we use a local mesh approach for constructing the Laplacian. We first approximate the local 1-ring neighborhood $N(v_i)$ of each point v_i by applying the 3D Delaunay triangulation method on \mathcal{P} and extracting the local connectivity. Using the local 1-ring neighborhoods, we can construct an $n \times n$ Laplacian matrix L using the cotangent formula [27], with its (i, j) -entry L_{ij} given by:

$$L_{ij} = \begin{cases} -\frac{1}{2}(\cot \alpha_{ij} + \cot \beta_{ij}), & \text{if } v_j \in N(v_i), \\ -\sum_{m \neq i} L_{im} & \text{if } j = i, \\ 0 & \text{otherwise,} \end{cases} \quad (1)$$

where α_{ij}, β_{ij} are the angles opposite to the edge $[v_i, v_j]$ in $N(v_i)$ (see [27] for more details). However, as the 3D Delaunay method produces a convex volume, certain points in \mathcal{P} may get omitted in the above computation. To resolve this issue, we use the modified local mesh method in [28] to handle the omitted vertices and approximate their local connectivity. More specifically, for each omitted vertex, we find its k -nearest neighbors and use the principal component analysis (PCA) to project them onto its tangent plane, where k is set to be 25 in practice. We can then approximate the local 1-ring neighborhood by constructing the 2D Delaunay triangulation for all the projected points. This allows us to compute the cotangent weights in Eq. (1) for the omitted points and incorporate them with L ,

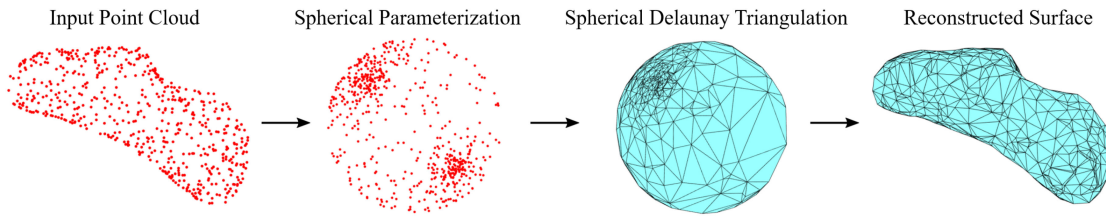


Fig. 1. Surface reconstruction via spherical parameterization. We first map the input point cloud to the unit sphere via a composition of several mappings and then apply the spherical Delaunay triangulation on the spherical parameterization, from which we obtain a reconstructed surface of the point cloud.

thereby getting an $n \times n$ modified Laplacian matrix \tilde{L} with all omitted points handled. Then, for any mapping $g : \mathcal{P} \rightarrow \mathbb{R}^2$, we can approximate the Laplacian Δ using \tilde{L} as follows:

$$\Delta g(v_i) = \sum_{v_j \in N(v_i)} \tilde{L}_{ij}(g(v_j) - g(v_i)), \quad (2)$$

where \tilde{L}_{ij} is the (i, j) -entry of \tilde{L} .

Now, we obtain a spherical parameterization of \mathcal{P} based on the approach in [29]. More specifically, we map \mathcal{P} onto a planar triangular domain by solving the Laplace equation:

$$\Delta g = 0. \quad (3)$$

Note that the above equation is an $n \times n$ sparse linear system and can be easily solved numerically using iterative methods. In the case that \mathcal{P} is too coarse or noisy such that the cotangent Laplacian causes degenerate solutions, we can simply remove the outlier points that form non-manifold geometry in the local mesh approximations and replace the cotangent Laplacian with the Tutte Laplacian [30], which is more robust to extreme angles in the local geometry. We then apply the inverse stereographic projection φ^{-1} to obtain a spherical parameterization:

$$\varphi^{-1}(x, y) = \left(\frac{2x}{1+x^2+y^2}, \frac{2y}{1+x^2+y^2}, \frac{-1+x^2+y^2}{1+x^2+y^2} \right), \quad (4)$$

where (x, y) are the Cartesian coordinates of a point on the 2D plane. Now, note that the composition $\varphi^{-1} \circ g$ (i.e. applying g followed by φ^{-1}) is a spherical parameterization that maps \mathcal{P} onto the unit sphere. As φ^{-1} is a conformal (angle-preserving) map and g is the solution of the Laplace equation (3), the spherical parameterization $\varphi^{-1} \circ g$ has low geometric distortion. To further improve the conformality of $\varphi^{-1} \circ g$, we apply the south-pole mapping scheme in [19], which involves computing another stereographic projection with respect to the south pole of the sphere and solving another Laplace equation with the outermost points fixed, followed by the inverse south-pole stereographic projection. Finally, we apply the Möbius area correction scheme in [31] to reduce the area distortion of the spherical parameterization. More specifically, we search for an optimal Möbius transformation $\tau(z) = \frac{az+b}{cz+d}$ (where a, b, c, d with $ad - bc \neq 0$ are the complex variables to be optimized) such that composing the spherical parameterization with $\varphi^{-1} \circ \tau \circ \varphi$ minimizes the average area distortion of all triangles in the local mesh approximation. Since Möbius transformations are conformal, the conformality of the parameterization will not be affected by this step. This completes the proposed spherical parameterization method for coarse point clouds.

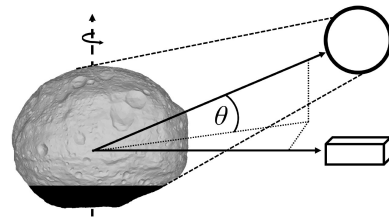


Fig. 2. Not to scale diagram showing the relative position of the spacecraft, small-body, and sun. The solar phase angle, θ , determines the region of the body permanently shadowed, shown by the black region.

With the spherical parameterization, we can directly apply the spherical Delaunay triangulation method [32] to construct a genus-0 triangular mesh of the unit sphere based on the parameterized points, which naturally induces a triangular mesh on the input point cloud \mathcal{P} . Note that the spherical Delaunay triangulation method ensures that the two angles α, β opposite to each edge on the sphere satisfy $\alpha + \beta \leq \pi$, which effectively reduces the occurrence of sharp triangles and hence maximizes the regularity of the triangulation. Since the distortion of the spherical parameterization is optimized in our proposed method, the induced triangulation on \mathcal{P} will also be highly regular. Moreover, as the topology of \mathcal{P} is preserved under the spherical parameterization, the reconstructed surface is guaranteed to be genus-0. Finally, we apply the edge flipping operator from [33] to minimize vertex curvature and smooth the reconstruction. As this only affects local connectivity, it does not introduce non-genus-0 features.

IV. SYMMETRY RECONSTRUCTION

Unlike planets, whose rotation axes are generally normal to their orbital plane, the “obliquity” of asteroids and comets tends to be totally random. As a result, seasonally, there can often be large regions of permanent shadow on the northern or southern hemispheres that are unobservable with visual sensors (see Fig. 2). Thus, the challenge of meshing sparse point clouds to form a global shape model can be exacerbated by large “holes” in the data set. Applying reconstruction algorithms directly to these point clouds results in a large planar region. However, we can leverage prior estimates of the pole orientation (e.g. through Silhouette methods [3]), the body’s centroid [1], and an assumption that small bodies often have a strong north-south *symmetry* in their shape to “fill in” large holes in point-cloud data as a preprocessing step to improve the robustness and accuracy of global shape reconstruction. This section describes our “symmetry reconstruction” algorithm. It differs from existing symmetry

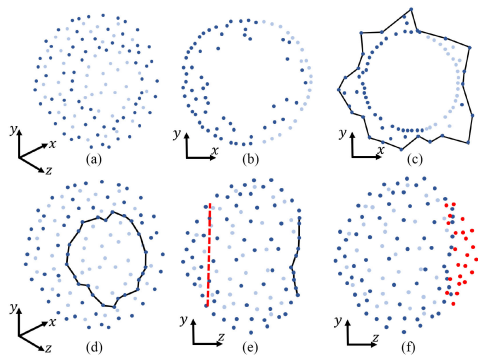


Fig. 3. Symmetry reconstruction steps applied to a simplified model of Vesta, (a) 3D point cloud, lighter colour indicates points on the far side of the body. (b) Planar projection of hemisphere containing the shadowed region. (c) Elliptical reflection of the planar projection with hole boundary marked. (d) 3D point cloud with hole boundary marked. (e) Side view of the 3D point cloud with hole boundary marked and mirror plane shown (red). (f) Side view of the 3D point cloud showing reflected points (red).

reconstruction methods due to the sparseness of information. The sparseness prevents methods that detect symmetry [24], [25]; instead, we rely on our initial assumption of north-south symmetry, similar to [23]. We separate this algorithm into two stages, boundary detection, and point mirroring.

A. Boundary Detection

Initially, we determine whether there is a permanently shadowed region using our knowledge of the sun location and pole estimate, shown in Fig. 2. We then identify which points lie on the boundary of this region. This is done by analysing the point cloud, prior to mapping, and leveraging an assumption that the rotation pole lies within the region.

Fig. 3 shows the steps for boundary detection of the shadowed region and symmetry reconstruction. Initially, we apply an orthographic projection along the z axis of the shadowed hemisphere, which we identify from the sun position, forming a 2D projection on the xy -plane.

Detecting the boundary points can be simplified by altering the point cloud so that the hole boundary lies on the exterior of the 2D projection. We do this by using least squares to fit an ellipse to the points of the orthographic projection. The major, a , and minor, b , axes of the ellipse are then used to generate an elliptical reflection, (x', y') , using Eq. (5):

$$x' = \frac{a^2 b^2 x}{b^2 x^2 + a^2 y^2}, \quad y' = \frac{a^2 b^2 y}{b^2 x^2 + a^2 y^2}. \quad (5)$$

With the bounding points of the shadowed region now at the edges of the elliptical reflection they are selected by computing the concave hull using a nearest neighbors approach [34]. This allows concavities in the boundary to be identified, as shown in Fig. 3(c).

B. Point Mirroring

After the boundary points of the hole are detected, they can be used to calculate mirror planes and determine which points should be reflected to fill the shadowed region with a

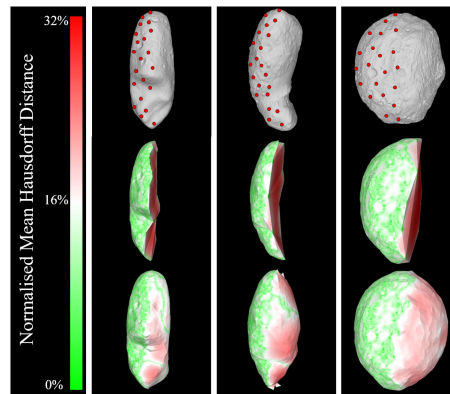


Fig. 4. Top row: Ground truth shape models for Eros, Itokawa, and Vesta, with sample landmarks for a 90° sun phase shown in red. Middle row: Reconstructions using original point clouds coloured with the Hausdorff distance. Bottom row: Reconstructions after applying symmetry assumptions coloured with the Hausdorff distance. The Hausdorff distance is normalized by the maximum diameter of the respective body.

TABLE I
COMPARISON OF SYMMETRY METRICS FOR THREE KNOWN BODIES

	Normalized Mean Distance (%)
Eros	1.11
Itokawa	3.17
Vesta	1.04

The distance is a metric for body symmetry through distance to a mirrored hemisphere. For comparison, each body is normalized by its maximum diameter. As expected from observation, Eros and Vesta are more symmetric than Itokawa.

symmetrical assumption. Initially we find the *nearest mirrored neighbors* for each of the boundary points. This is done for each boundary point, $X = (x, y, z)$, by finding the point on the opposite hemisphere, $X_i = (x_i, y_i, z_i)$, which minimizes the distance function:

$$d(X, X_i) = \sqrt{w_x(x - x_i)^2 + w_y(y - y_i)^2 + w_z(z + z_i)^2}. \quad (6)$$

Where we set $w_x = w_y = 9$ and $w_z = 1$, this difference in weighting is because the best plane of symmetry may not be the body equatorial plane. Minimizing the z -component avoids this simplification and emphasizing x and y improves the continuity between the mirrored and measured points.

After defining these mirror planes, one at the border of the shadowed region and one on the visible hemisphere of the body (Fig. 3(e)), the relative position of all points lying above the visible plane are found. These points are then reflected and rotated to align with the other plane. The result is a symmetry estimated point cloud of the body (Fig. 3(f)).

As shown in Fig. 4, small bodies have varying levels of symmetry, affecting the accuracy of the reconstruction method described above. This fact is further shown in Table I, where the symmetry of each example body is analyzed with a metric similar to that proposed by Alvin *et al.* [23].

V. TESTING METHOD

To analyse the performance of the proposed surface reconstruction algorithm we require point clouds and ground-truth

information for a range of conditions. We generate these by computing the observability of points on the body, using this to generate a realistic sample.

To determine landmark observability we apply the Hidden Point Removal (HPR) operator, introduced by Katz *et al.* [35], to high-resolution models of small bodies. These initial shape models are normalized by their maximum diameter, to allow scale-independent comparisons. The HPR operator allows us to find which points are both illuminated and in view of the spacecraft. Simulating this over a full rotation of the body and tracking each points visibility, allows an output point cloud to be selected probabilistically. Selecting point clouds with this method, as opposed to a feature tracking method, isolates the reconstruction error from any landmark errors that could be introduced.

All test data presented in this paper simulates a spacecraft performing a hover directly above the equator of the small body (Fig. 2). The distance of the spacecraft from the body was chosen to be 100 times the body maximum diameter, consistent with distances that feature tracking may be performed [1]. To test the performance of the symmetry reconstruction method, we vary the sun elevation.

We define a Sun Phase Angle, shown in Fig. 2, which describes the elevation between the spacecraft and the sun in the small-body-centered inertial frame. For example, zero phase angle has the sun directly behind the spacecraft.

Eros, Itokawa, and Vesta were the primary small bodies chosen for analysis as they are representative of typical asteroids that might be encountered. They also display varying shape aspects such as high curvature, concave regions, and differing levels of symmetry, as shown in Table I. Additionally, they benefit from being extensively studied, enabling access to high-resolution shape files that were used to generate test datasets. The analysis presented here was conducted on sampled point clouds of 100–1000 points, in 100 point increments, and sun phase angles of $15^\circ \rightarrow 90^\circ$, in 5° increments. Five point clouds were generated for each scenario resulting in 800 unique point clouds for each body. All algorithms were then tested on the same point clouds with results averaged for each scenario. The minimum sun phase angle was limited to 15° as smaller angles resulted in a shadowed region that was often too small for hole detection at low point densities. The performance increase of the symmetry reconstruction was also found to be negligible at such small sun phase angles.

To analyse the accuracy of reconstructions, we use the volumetric error to ground truth and the mean Hausdorff distance [36] normalized by the maximum diameter of the ground-truth body. The Hausdorff distances between the reconstructed surface and the ground truth, are the minimum distance between the reconstructed vertices and those of the ground-truth model. The mean Hausdorff distance is a widely used metric for reconstruction accuracy. Normalizing by the ground-truth diameter gives a dimensionless parameter for comparison across different bodies. Volumetric error is considered as it is the main measure for accuracy of a gravity estimate, a primary motivator for coarse shape models.

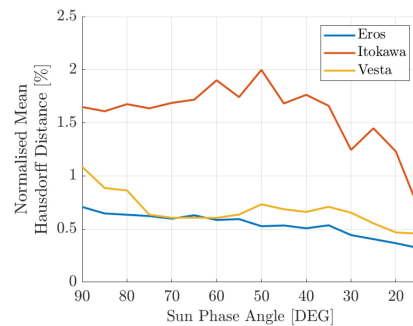


Fig. 5. Comparison of normalized mean Hausdorff distance for varying bodies with symmetry hole filling applied for 1000 point datasets.

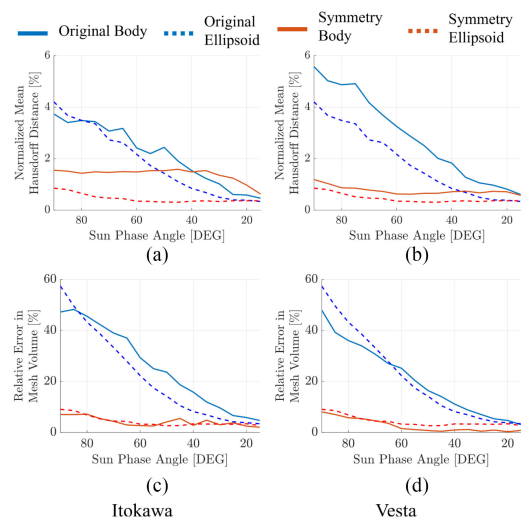


Fig. 6. Effect of symmetry hole filling applied to 400 point reconstructions of Itokawa, (a) and (c), and Vesta, (b) and (d). With results compared to a perfect ellipsoid.

VI. RESULTS

We independently assess the performance of the mapping algorithm with and without applying symmetry reconstruction. We then analyze the performance of our parameterization algorithm on the symmetry reconstructed datasets, with comparison to state-of-the-practice methods.

A. Symmetry Reconstruction

We analyze the performance of the symmetry method for different small bodies with varying sun-phase angles. We find that even on Itokawa, symmetry reconstruction has benefits for shape reconstruction.

Fig. 5 compares the mean Hausdorff distance for reconstructed bodies using the parameterization algorithm with the symmetric method for 1000-point datasets. Fig. 5 shows consistent results with Table I: Eros and Vesta performing similarly and much better than Itokawa. The improved performance on Eros over Vesta may result from the larger surface area of Vesta, which leads to lower density of points.

Fig. 6(b) and 6(d) show that applying symmetry reconstruction on bodies with high symmetry, such as Vesta, substantially

TABLE II
SUMMARY OF COARSE 3D MAPPING METHODS

	Doesn't Require Point Normals	Faithful Recon	Enforce Genus-0
Tight Cocone [14]	yes	yes	no
Powercrust [15]	yes	yes	no
Screened Poisson [37]	no	no	no
Spherical Parameterization	yes	yes	yes

improves reconstruction accuracy for all cases above our 15° cut-off. This is further shown on a perfectly symmetrical ellipsoid, demonstrating the efficacy of the method. The results on a less-symmetric body, Itokawa, are shown in Fig. 6(a) and 6(c). We see that reconstruction accuracy suffers below 40°, however volume error is still improved after applying symmetry. For applications of coarse maps to gravity estimation, volume error is more important, hence we favor the use of the symmetry assumption for coarse shape generation.

B. Genus-0 Reconstructions

We present analysis of the proposed parameterization algorithm against the state-of-the-practice. For comparison we select three common algorithms, Screened Poisson Surface Reconstruction [37], Powercrust [15], and Tight Cocone [14]. They were primarily chosen as they enforce watertight reconstructions, a requirement for asteroid shape models.

A summary of key aspects of the reconstruction algorithms is shown in Table II. While Tight Cocone and Powercrust use spatial representations of the Voronoi diagram, Screened Poisson Surface Reconstruction is a representation of the implicit surface defined by the gradient function of the point normals. The calculation of this implicit surface can be adjusted with a range of parameters, which require tuning based on the point cloud. To address the different point densities, we apply two sets of tuning parameters. The main change between these variations is the degree of the B-spline used to estimate the indicator function. A higher degree B-spline was used for very sparse data, as it produces a smooth interpolation across undersampled regions. Additionally, the resolution of the voxel grid used to compute the surface was adjusted. Computing the solution with larger voxels improved the reconstruction for sparse data, but excessively smoothed the shape at higher densities. In both cases, the final reconstruction was still represented at the same resolution.

The main benefit of the proposed parameterization algorithm over existing methods is the enforcement of genus-0 reconstruction. While existing algorithms can enforce watertight reconstructions, they do not have any guarantees for the genus of the output. For a mapping scenario where the body is known to be genus-0, this is a valuable constraint. Especially for coarse reconstructions, robustness of shape consistency is preferable to a slight increase in accuracy. As such, for our comparison, in addition to the mean Hausdorff distance and volume error, we add a third metric of the number of non-genus-0 reconstructions. More specifically, for a genus-0 surface with v vertices, e edges and f faces, we must have $v - e + f = 2$. Therefore, by computing the value of $v - e + f$ for the surfaces reconstructed

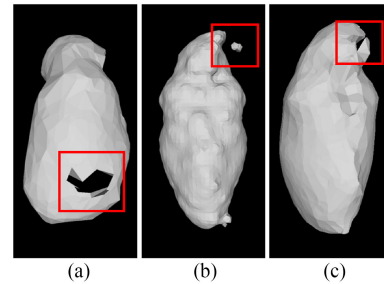


Fig. 7. Examples of reconstructions that are not genus-0. (a) Powercrust and Cocone both showed reconstructions with a hole passing through the mesh. (b) Poisson would create multiple volumes for a single reconstruction. (c) Powercrust generated multiple non-genus-0 shapes at reflected point discontinuities on Itokawa (top right).

TABLE III
GENUS-0 RECONSTRUCTIONS FROM 800 POINT CLOUDS PER BODY

	Eros	Itokawa	Vesta
Cocone	99.7%	99.7%	100%
Powercrust	97.6%	76%	99.5%
Poisson Coarse	100%	99.2%	100%
Poisson Dense	78.9%	32.8%	72.9%
Spherical Param	100%	100%	100%

by different methods, we can count the number of non-genus-0 reconstructions.

While not always common, existing algorithms all showed multiple reconstructions that were not genus-0.¹ Examples of these are shown in Fig. 7. Powercrust and Cocone both exhibited non-genus-0 reconstructions due to holes passing through the body (Fig. 7(a)). Poisson, however, creates separate volumes around isolated points (Fig. 7(b)). These can easily be removed in a clean-up step, however, they are included as non-genus-0 reconstructions due to the loss of information. While this behaviour was greatly reduced with the coarse tuning parameters, it still occurred for some reconstructions of Itokawa. It should be noted that these results are collected from symmetry reconstructed datasets, so are influenced by the symmetry assumption.

Table III shows that our parameterization method is the only algorithm to always produce genus-0 reconstructions. While Cocone produced the least non-genus-0 reconstructions, the ones it produced, as shown in Fig. 7(a), result in inaccurate shape models. Fewer genus-0 reconstructions were produced for Itokawa, due to its low symmetry causing sharp changes between mirrored and measured points. Poisson, with dense tuning parameters, and Powercrust were the most affected, regularly producing the results shown in Fig. 7(b) and 7(c) respectively.

As mentioned earlier, the prior parameterization-based method [19] relies on the MLS method for approximating the Laplacian and does not work well for coarse point clouds. Fig. 8 shows several point clouds and the surface reconstructions produced by our method and the method [19]. It can be observed that

¹It should be noted that Cocone and Powercrust occasionally produce a non-watertight mesh, however in these cases the hole was bordered by three vertices, meaning a simple hole closing algorithm could repair the mesh by adding the missing face. As this is a trivial clean-up step, these were not counted among non-genus-0 reconstructions

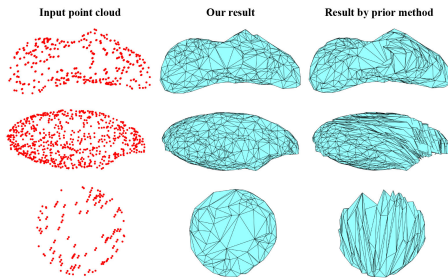


Fig. 8. Surface reconstruction results produced by our method and the prior spherical parameterization method [19]. The three example point clouds are from Eros, Itokawa, and Vesta respectively.

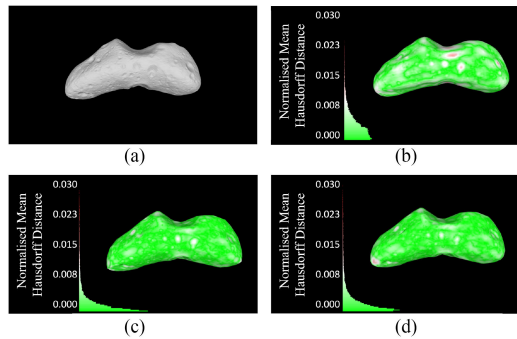


Fig. 9. Visual comparison of reconstructions of Eros with 800 points and 15° sun phase, with the distribution of the Hausdorff distance shown. (a) Ground Truth, (b) Poisson, (c) Powercrust, and (d) Spherical Parameterization.

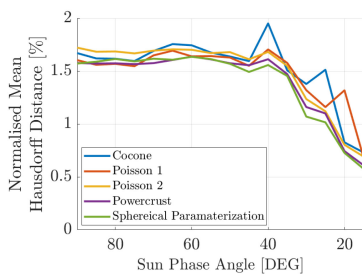


Fig. 10. Accuracy of reconstructions of Itokawa with 800 points.

the poorly approximated Laplacian in [19] leads to highly distorted triangulations. By contrast, our method produces meshes with much better triangle quality.

C. Reconstruction Accuracy

Here we assess the accuracy of reconstructions with our parameterization algorithm compared to the state-of-the-practice, and showcase the effect of non-genus-0 reconstructions. To independently assess the parameterization, symmetry reconstruction is applied for all algorithms. Fig. 9 shows reconstructions of the same point cloud with different algorithms. The difference between faithful reconstructions, Fig. 9(c) and 9(d), and implicit reconstructions, Fig. 9(b), can be seen both visually, and through the distribution of the Hausdorff distance, shown in Fig. 9.

The effect of the non-genus-0 reconstructions can be seen clearly in the performance of the Cocone algorithm in Fig. 10. The sharp peaks in Hausdorff distance at 25° and 40° are caused by shape models which had holes passing through them, as in Fig. 7(a). The main advantage of the parameterization algorithm

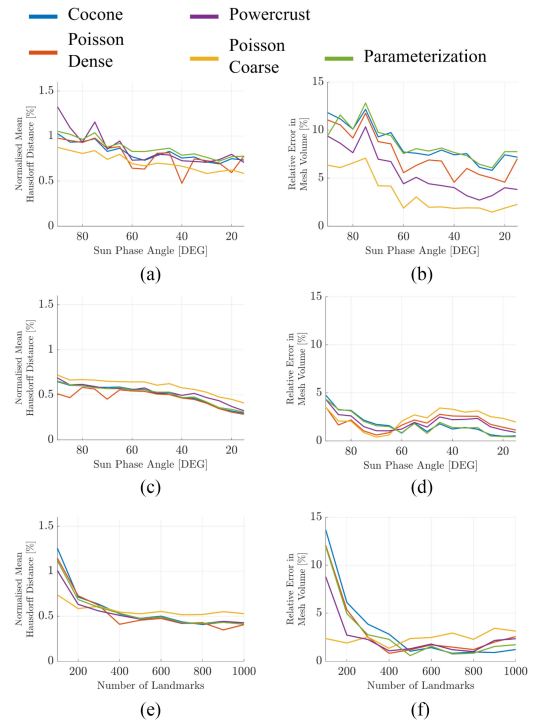


Fig. 11. Accuracy of Eros reconstructions using each algorithm and the symmetry method. (a) Mean Hausdorff distance with 200 points. (b) Volume error with 200 points. (c) Mean Hausdorff distance with 1000 points. (d) Volume error with 1000 points. (e) Mean Hausdorff distance with 30° sun phase. (f) Volume error with 30° sun phase.

is that it avoids this behaviour, resulting in more consistent performance across a range of conditions, leading to higher confidence in the shape model. Additionally, Fig. 10 shows the reconstruction accuracy increasing as the solar phase decreases. This is due to the increased visibility of the body, leading to less of the body being reconstructed through symmetry; this result is consistent with Fig. 6(c).

Fig. 11 shows the performance of all algorithms on reconstructions of Eros with 200 and 1000 point clouds with symmetry applied. Generally, consistent performance among algorithms is observed, especially for dense data, as shown in Fig. 11(c). As expected we see that the coarse tuning for Screened Poisson Reconstruction is the most consistent performer at 200 points, however performs poorly at 1000 points due to excessive smoothing. We typically see correlation between the faithful (parameterization and Tight Cocone) and interpolating (Powercrust and Poisson) algorithms as the shape models contain the same vertices, with only connectivity varying between results. Being constructed from an implicit function, the results from Poisson display more variability, noticeable in Fig. 11(a) and 11(c) with sudden drops in Hausdorff distance. It should be noted this variability has been observed to cause decreases, Fig. 11(a) and 11(c), and increases, Fig. 10 at 20° , in the mean Hausdorff distance.

While Fig. 11 shows that parameterization performs consistently with existing algorithms, we demonstrate this further by looking at all the reconstructions of Itokawa, with varying point density and sun phase angle. Fig. 12 shows the same behaviour as Fig. 11(d), where parameterization is among the

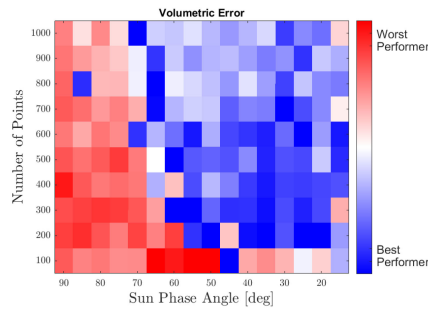


Fig. 12. Comparison of reconstruction volume error between spherical parameterization and existing algorithms. Shown with a linear color scale bounded by the best and worst performing algorithm for each condition.

best performers at low sun phase, but degrades relative to the best performing alternative at high sun phase. We also see that parameterization performs better with increasing point density. This is not surprising given the increased mesh vertices from its faithful reconstruction begin to gain similar resolution to the interpolation algorithms. The poor relative performance at high phase angles could be due to inaccuracies in the mirrored points, which become more noticeable on a faithful reconstruction.

VII. CONCLUSION

Generating a shape model of a small body from sparse feature tracked points presents a number of difficulties. This letter addresses these by presenting a spherical parameterization algorithm that can robustly generate water-tight genus-0 shape models and handle permanently shadowed regions using symmetry assumptions. The approach to address permanent shadows was shown to improve volumetric error in all cases, even for a low-symmetry body when the mean Hausdorff distance increased at high sun phase. Our combined approach is a method for shape reconstruction from sparse landmarks which guarantees consistent topology without sacrificing accuracy compared to the state-of-the-practice.

REFERENCES

- [1] I. A. D. Nesnas *et al.*, "Autonomous exploration of small bodies toward greater autonomy for deep space mission," *Front. Robot. AI*, 2021.
- [2] B. J. Morrell *et al.*, "Autonomous feature tracking for autonomous approach to a small body," in *ASCEND 2020*, 2020, p. 4151, Paper 2020-4151.
- [3] S. Bandyopadhyay *et al.*, "Light-robust pole-from-silhouette algorithm and visual-hull estimation for autonomous optical navigation to an unknown small body," in *Proc. 31st AAS/AIAA Space Flight Mechanics Meeting*, 2021, pp. 1–13.
- [4] D. N. DellaGiustina *et al.*, "Overcoming the challenges associated with image-based mapping of small bodies in preparation for the osiris-rem mission to (101955) bennu," *Earth Space Sci.*, vol. 5, no. 12, pp. 929–949, 2018.
- [5] R. W. Gaskell *et al.*, "Characterizing and navigating small bodies with imaging data," *Meteorit. Planet. Sci.*, vol. 43, no. 6, 2008.
- [6] O. S. Barnouin *et al.*, "Digital terrain mapping by the OSIRIS-REx mission," *Planet. Space Sci.*, vol. 180, 2020, Art. no. 104764.
- [7] C. Cocard and T. Kubota, "SURF-based SLAM scheme using octree occupancy grid for autonomous landing on asteroids," in *Proc. 10th Int. Symp. Artif. Intell., Robot. Automat. Space*, vol. 29, 2010, pp. 275–282.
- [8] N. Takeishi and T. Yairi, "Dynamic visual simultaneous localization and mapping for asteroid exploration," in *Proc. I-Sairas Beijing*, 2016.
- [9] A. Rathinam and A. G. Dempster, "3D reconstruction of an asteroid shape using visual SLAM for autonomous navigation," in *Proc. 17th Australian Space Res. Conf.*, 2017, pp. 87–96.

- [10] H. Hoppe, T. DeRose, T. Duchamp, J. McDonald, and W. Stuetzle, "Surface reconstruction from unorganized points," in *Proc. 19th Annu. Conf. Comput. Graph. Interactive Techn.*, 1992, pp. 71–78.
- [11] M. S. Floater and M. Reimers, "Meshless parameterization and surface reconstruction," *Comput. Aided Geom. Des.*, vol. 18, no. 2, pp. 77–92, 2001.
- [12] G. Tewari, C. Gotsman, and S. J. Gortler, "Meshing genus-1 point clouds using discrete one-forms," *Comput. Graph.*, vol. 30, no. 6, pp. 917–926, 2006.
- [13] T. K. Dey and J. Giesen, "Detecting undersampling in surface reconstruction," in *Proc. 17th Annu. Symp. Comput. Geometry*, 2001, pp. 257–263.
- [14] T. K. Dey and S. Goswami, "Tight cocone: A water-tight surface reconstructor," *J. Comput. Inf. Sci. Eng.*, vol. 3, no. 4, pp. 302–307, 2003.
- [15] N. Amenta, S. Choi, and R. K. Kolluri, "The power crust," in *Proc. 6th ACM Symp. Solid Model. Appl.*, 2001, pp. 249–266.
- [16] M. Kazhdan, M. Bolitho, and H. Hoppe, "Poisson surface reconstruction," in *Proc. 4th Eurographics Symp. Geometry Process.*, 2006, vol. 7, pp. 61–70.
- [17] M. Zwicker and C. Gotsman, "Meshing point clouds using spherical parameterization," in *Proc. Eurographics Symp. Point-Based Graph.*, 2004, pp. 173–180.
- [18] T. W. Meng, G. P. -T. Choi, and L. M. Lui, "TEMPO: Feature-endowed teichmüller extremal mappings of point clouds," *SIAM J. Imag. Sci.*, vol. 9, no. 4, pp. 1922–1962, 2016.
- [19] G. P.-T. Choi, K. T. Ho, and L. M. Lui, "Spherical conformal parameterization of genus-0 point clouds for meshing," *SIAM J. Imag. Sci.*, vol. 9, no. 4, pp. 1582–1618, 2016.
- [20] C. Bartalucci, R. Furferi, L. Governi, and Y. Volpe, "A survey of methods for symmetry detection on 3D high point density models in biomedicine," *Symmetry*, vol. 10, no. 7, p. 263, 2018.
- [21] Y. Zhou, S. Liu, and Y. Ma, "Learning to detect 3D reflection symmetry for single-view reconstruction," 2020, *arXiv:2006.10042*.
- [22] A. Davidescu and G. Savii, "Planar robot grasping planning based on symmetry," *Appl. Mech. Mater.*, vol. 658, pp. 593–598, Oct. 2014.
- [23] L. Alvin and J. A. G. Daniel, "Single viewpoint model completion of symmetric objects for digital inspection," *Comput. Vis. Image Underst.*, vol. 115, no. 5, pp. 603–610, 2011.
- [24] R. Nagar and S. Raman, "Detecting approximate reflection symmetry in a point set using optimization on manifold," *IEEE Trans. Signal Process.*, vol. 67, no. 6, pp. 1582–1595, Mar. 2019.
- [25] S. Thrun and B. Wegbreit, "Shape from symmetry," in *Proc. 10th IEEE Int. Conf. Comput. Vis.*, 2005, pp. 1824–1831.
- [26] F. Preusser *et al.*, "Shape model, reference system definition, and cartographic mapping standards for comet 67p/churyumov-gerasimenko-stereo-photogrammetric analysis of rosetta/osiris image data," *Astron. Astrophys.*, vol. 583, p. A 33, 2015.
- [27] U. Pinkall and K. Polthier, "Computing discrete minimal surfaces and their conjugates," *Exp. Math.*, vol. 2, no. 1, pp. 15–36, 1993.
- [28] Y. Liu, G. P. T. Choi, and L. M. Lui, "Free-boundary conformal parameterization of point clouds," 2020, *arXiv:2010.15399*.
- [29] P. T. Choi, K. C. Lam, and L. M. Lui, "FLASH: Fast landmark aligned spherical harmonic parameterization for genus-0 closed brain surfaces," *SIAM J. Imag. Sci.*, vol. 8, no. 1, pp. 67–94, 2015.
- [30] W. T. Tutte, "How to draw a graph," *Proc. London Math. Soc.*, vol. 3, no. 1, pp. 743–767, 1963.
- [31] G. P. T. Choi, Y. Leung-Liu, X. Gu, and L. M. Lui, "Parallelizable global conformal parameterization of simply-connected surfaces via partial welding," *SIAM J. Imag. Sci.*, vol. 13, no. 3, pp. 1049–1083, 2020.
- [32] C. D. Toth, J. O'Rourke, and J. E. Goodman, in *Handbook of Discrete and Computational Geometry*. Boca Raton, FL, USA: CRC press, 2017.
- [33] N. Dyn, K. Hormann, S.-J. Kim, and D. Levin, "Optimizing 3D Triangulations Using Discrete Curvature Analysis. 1st ed. USA: Vanderbilt Univ., 2001, pp. 135–146.
- [34] A. Moreira and M. Santos, "Concave hull: A k-nearest neighbours approach for the computation of the region occupied by a set of points," in *Proc. 2nd Int. Conf. Comput. Graph. Theory Appl.*, Jan. 2007, pp. 61–68.
- [35] S. Katz, A. Tal, and R. Basri, "Direct visibility of point sets," *ACM Trans. Graph.*, vol. 3, p. 24, 2007.
- [36] E. Oniga and C. Chirila, "Hausdorff distance for the differences calculation between 3D surfaces," *J. Geodesy Cadastre RevCAD*, vol. 15, pp. 193–202, 2013.
- [37] M. Kazhdan and H. Hoppe, "An adaptive multi-grid solver for applications in computer graphics," *Comput. Graph. Forum*, vol. 38, no. 1, pp. 138–150, 2019.